Resilient High Catalytic Performance of Platinum Nanocatalysts with Porous Graphene Envelope

Heeyeon Kim,*,† Alex W. Robertson,*,‡ Sang Ouk Kim,§ Jong Min Kim,‖ and Jamie H. Warner‡

†Energy Materials Laboratory, Korean Institute of Energy Research, 152 Gajeong-ro, Yuseong-gu, Daejeon 305-343, Korea, ‡Department of Materials, University of Oxford, Parks Road, Oxford OX1 3PH, United Kingdom, §Department of Materials Science and Engineering, KAIST, 291 Daehak-ro, Yuseong-gu, Daejeon 305-701, Korea, and ‖Department of Engineering, University of Oxford, Parks Road, Oxford OX1 3PJ, United Kingdom

ABSTRACT Despite the innumerable developments of nanosized and well dispersed noble metal catalysts, the degradation of metal nanoparticle catalysts has proven to be a significant obstacle for the commercialization of the hydrogen fuel cell. Here, the formation of Pt nanoparticle catalysts with a porous graphene envelope has been achieved using a single step low temperature vaporization process. While these Pt–Gr core–shell nanoparticles possess superior resilience to degradation, it comes at the cost of degraded overall catalyst efficacy.

However, it is possible to combat this lower overall performance through inclusion of low concentrations of nitrogen precursor in the initial stage of single-step synthesis, inhibiting the formation of complete graphene shells, as verified by atomic resolution aberration-corrected transmission electron microscopy (AC-TEM) imaging. The resultant porous graphene encapsulated Pt catalysts are found to have both the high peak performance of the bare Pt nanoparticle catalysts and the increased resilience of the fully shielded Pt–Gr core–shells, with the optimal N-doped Pt–Gr yielding a peak efficiency of 87% compared to bare Pt, and maintaining 90% of its catalytic activity after extended potential cycling. The nitrogen treated Pt–Gr core–shells thus act as an effective substitute catalyst for conventional bare Pt nanoparticles, maintaining their catalytic performance over prolonged use.
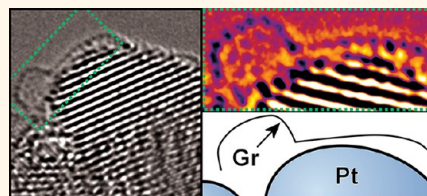
KEYWORDS: platinum · catalysis · graphene · TEM · nanoparticle · fuel cells

The demand for low-carbon emission, efficient and mobile power sources suitable for locomotive, domestic and device applications has led to intense research efforts for the alternative energy storage schemes beyond traditional hydrocarbon combustion. A leading candidate is the proton exchange membrane fuel cell (PEMFC), but the utilization of costly noble metal catalysts, including platinum, has precluded the use of this technology other than for niche applications. There are two potential routes to challenge this inherent problem: to explore alternative, economically viable catalyst materials,[1-4] or to adapt the existing noble metal scheme with improved efficiency and reduced cost. More specifically, long-term catalytic efficiency can be greatly improved by addressing the typical degradation mechanisms of catalysts, such as agglomeration, dissolution into the electrolyte, poisoning of catalytic sites and degradation of the catalytic support.[5-7]

It is possible to combine Pt with other metals to improve the overall performance and durability. Previous approaches have included alloying Pt alloys with other transition metals, such as Co, Cu and Fe,[8-15] or core–shell structure formation with atomic thick Pt shells.[16-18] Alternatively, the stability of the metal catalyst particles can be improved through their encapsulation by well-defined carbon layers, which limit the catalytic degradation by detachment, dissolution and sintering.[19] In this work, we report the development of a graphene encapsulated Pt nanoparticle, or Pt–Gr core–shell, which demonstrates increased long-term activity and stability when deployed as a catalyst for PEMFCs. The graphene shell ranges from one to several layers, and is able to be synthesized at low temperatures of 400 °C through a single-step process. We find that the graphene shells protect the Pt cores from the hostile operating conditions of a fuel cell and, by including low concentration of nitrogen during synthesis, is still able to perform its role as a catalyst effectively. Through characterization by aberration corrected transmission electron

©2015 American Chemical Society

microscopy (AC-TEM), we examine the sensitivity of the degree of graphene crystallinity and layer thickness to the synthesis conditions, and relate these findings to electrochemical performance measurements.

RESULTS AND DISCUSSION

The Pt−Gr core−shells were synthesized by the simultaneous vaporization of carbon and Pt precursors, as shown in Figure 1a, at temperatures ranging from 400 to 1100 °C. At these elevated temperatures, catalytic growth of graphene occurs at the Pt nanoparticle surface.[20−22] Platinum catalyzed growth of graphene proceeds in a similar manner to that of copper, with the low carbon solubility of the metal presenting a dissociation limited growth regime where the supply of carbon reactant to the metal surface is the rate-controlling step; this is the ideal mode for the growth of mono- to few-layer graphene films,[23] making Pt an effective catalyst for high quality graphene growth.[20] SEM imaging demonstrated successful deposition of the Pt−Gr nanoparticles on carbon paper (Supporting Information Figure S1). X-ray diffraction (Supporting Information Figure S2) detects the typical lattice spacing for graphite and Pt(111), as well as some traces of Pt(200) and Pt(220). The growth of graphene on the Pt was confirmed by AC-TEM inspection. Figure 1b,c shows typical AC-TEM images of Pt nanoparticles encapsulated with graphene layers. It is possible to directly relate the number of contrast fringes to the graphene layer count.[24] For instance, the Pt−Gr in Figure 1c is coated by two layers, with an additional third layer marked by a green arrow. Box averaged intensity profiles taken orthogonally across the shell (Figure 1d) demonstrate the layer number, with the interlayer spacing between the minima measured at 3.4 ± 0.3 Å, in good agreement with the experimental results for free-standing few-layer graphene films.[25]

The synthesis temperature, along with the type of carbon precursor, is one of the principal processing variables for graphene encapsulation. For a better understanding of the role of temperature, noncorrected high resolution (HR-)TEM imaging and Raman spectroscopy were performed on the samples synthesized at various temperatures. A representative selection of HR-TEM images and Raman spectra for samples synthesized from ethanol precursor are presented in Figure 2. The HR-TEM images show an overall increase in graphene shell number from ∼1 to 2 for 400−600 °C
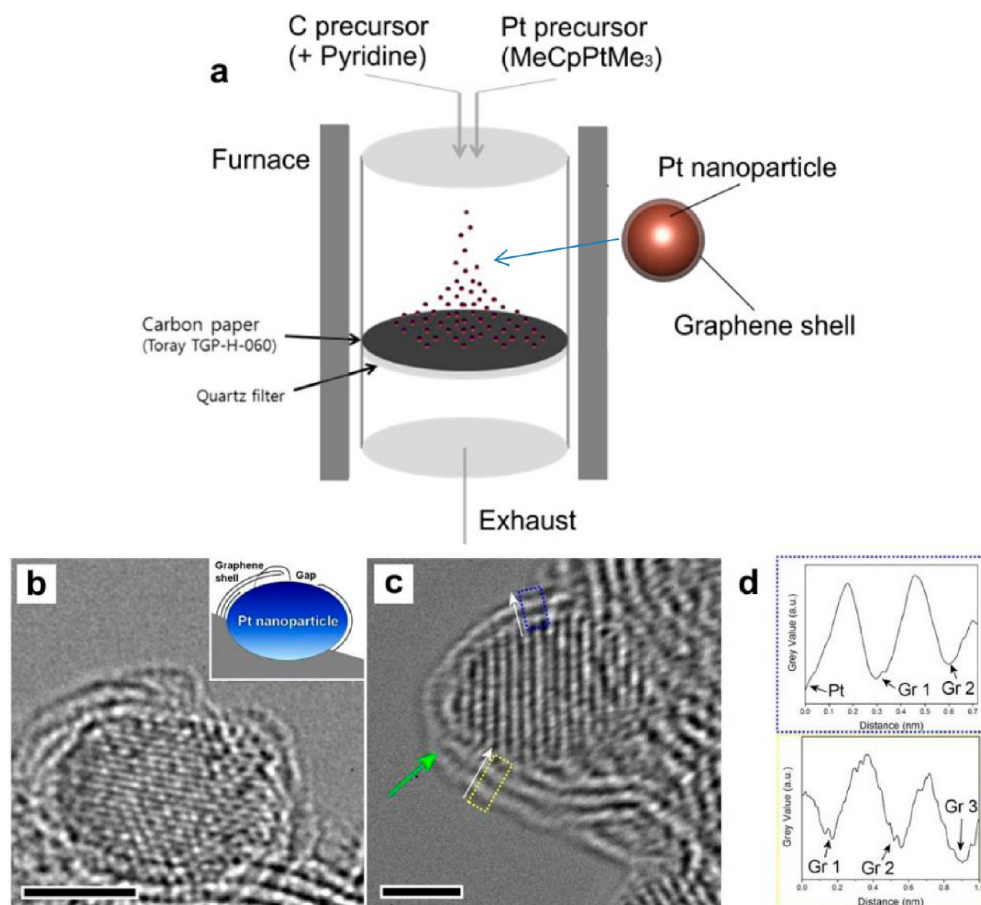

Figure 1. (a) Schematic illustration of the chemical vapor deposition growth of Pt nanoparticle catalysts encapsulated with graphene layers. (b) AC-TEM image of a Pt−Gr core−shell with a gap in the graphene shell coverage. (c) AC-TEM image of a Pt−Gr core−shell with varying layer counts. Scale bars 2 nm. (d) Box averaged intensity line profiles taken from the appropriately colored boxes in (c), with the positive x axis direction indicated by the arrows.
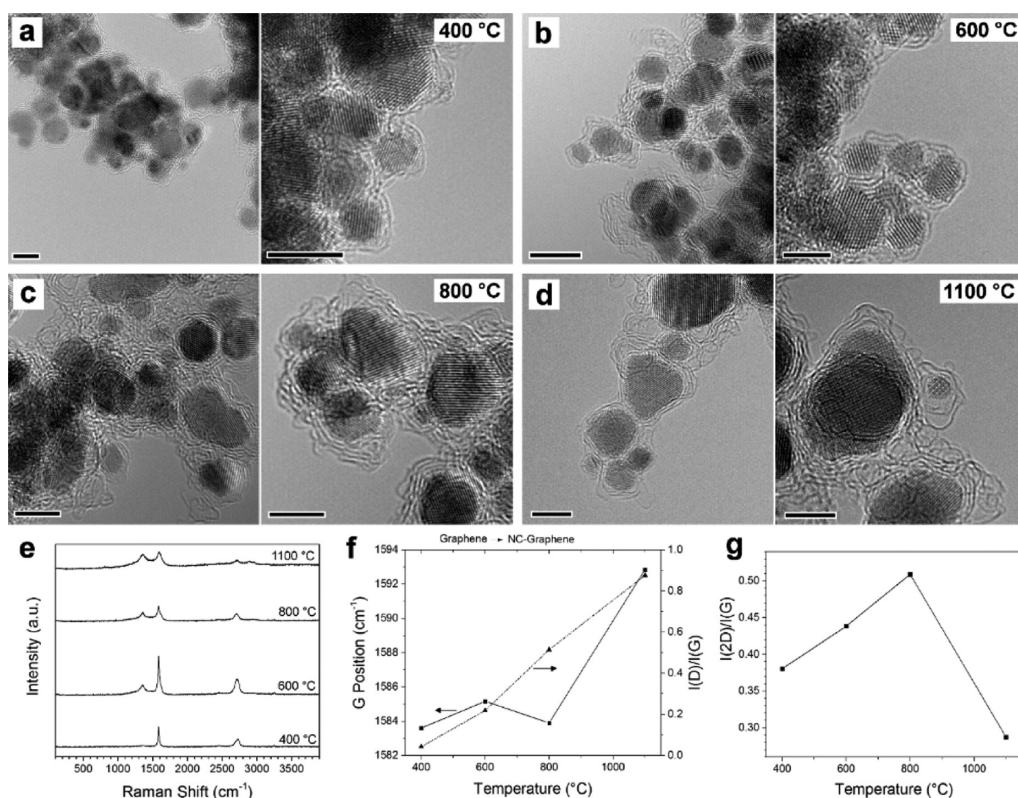
Figure 2. Effect of synthesis temperature on Pt—Gr core—shell structure formation (ethanol precursor). (a—d) HR-TEM images of Pt—Gr core—shells synthesized at 400, 600, 800, and 1100 °C, respectively. Scale bar 5 nm. (e) Raman spectra for 400, 600, 800, and 1100 °C. Effects of synthesis temperature on (f) Raman G peak position and D/G peak intensity ratio and (g) 2D/G peak intensity ratio.

(Figure 2a,b) to predominantly ~3 for 800—1100 °C (Figure 2c,d). Average nanoparticle size also increases with temperature, suggesting that notable particle sintering occurs prior to, or in parallel with, graphene growth at a high temperature.

The Raman spectra for growth temperatures of 400, 600, 800, and 1100 °C were taken with different carbon precursors. Figure 2e show the results for the ethanol precursor. These spectra show the D and G peaks characteristic of carbon compounds at their expected wavenumbers, as well as a 2D peak at some temperatures that is indicative of sp^2 carbons.[26] Detailed analysis of the spectra with Lorentz fitting clarifies the exact G peak position. The relative intensities of D and 2D peaks with respect to the G peak may quantify the crystallinity of the carbon shells. Figure 2f,g demonstrates the optimal synthesis temperature found to be 400 °C. The low $I(D)/I(G)$ peak intensity ratio and G peak wavenumber near 1580 cm^{-1} are the typical characteristics of well crystallized graphite. The moderate $I(D)/I(G)$ intensity ratio is indicative of few-layer graphene.[27] The increases in wavenumber and $I(D)/I(G)$ suggest a shift toward growth of nanocrystalline graphene at higher temperatures, and the sudden increases in $I(D)/I(G)$ and G peak position indicate that graphitic carbon barely remains at 1100 °C.[26,28] Raman analysis for other carbon precursors (Supporting

Information Figure S3) shows optimum growth temperatures of between 400 and 600 °C.

While it can be expected that the graphene shell would act to protect the Pt core, a completely covered Pt surface would be detrimental to the catalytic performance due to the screening of active sites. It is therefore important to control the level of graphene coverage and the defects in the graphene shell, such that an optimum compromise between catalyst stability and activity may be found. To achieve this, we covaporized a nitrogen precursor, pyridine, alongside the carbon precursor to form partially complete graphene shells. Through control of the relative concentration of nitrogen precursor, it was anticipated that the graphene shell would be more porous, *i.e.*, possess suitably large gaps in the shell, to permit molecular reactants to reach the Pt surface. To better understand the effect of nitrogen precursor and synthesis temperature on the as-grown graphene shells, we performed high resolution AC-TEM on the Pt—Gr samples prepared with an ethanol carbon precursor.

The influence from synthesis temperature on the graphene shell crystallinity and thickness is illustrated through representative AC-TEM images of samples synthesized at 400, 600, and 800 °C in Figure 3a—c, respectively. For the 400 °C sample (Figure 3a), Pt particles are exclusively covered with monolayer
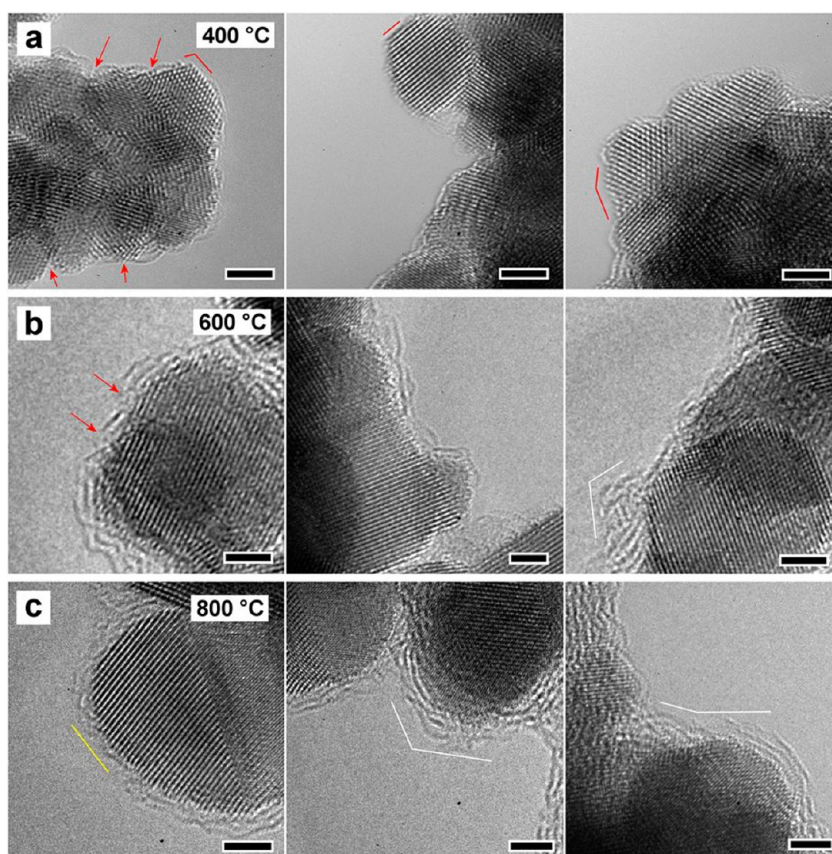
Figure 3. AC-TEM images demonstrating the typical Pt−Gr structures obtained at (a) 400 °C, (b) 600 °C, and (c) 800 °C, respectively. All samples were synthesized with a nitrogen precursor concentration of 0.5% by volume. Red annotations denote partially complete graphene shells, leaving bare Pt surface exposed. Yellow denotes the incomplete outer graphene layer, where Pt surface is still covered by inner layers. White indicates areas of amorphous coverage. Scale bars are 2 nm.

graphene, with the graphene forming encapsulation envelopes over small clusters of Pt nanocrystals. More detailed examination reveals some regions where the Pt surface is exposed, with partial graphene coverage evident for either small points (red arrows) or along extended stretches (red lines). For the 600 °C sample (Figure 3b), Pt nanocrystals with thicker multilayer shells are observed. The thicker coating was still observed to have a few regions where the Pt surface was exposed; however, it was significantly less frequent than for the monolayer encapsulation case of particles synthesized at 400 °C. Significantly, thick encapsulation layers are observed to have a low crystallinity, as indicated by white annotations in Figure 3. These portions appear predominantly amorphous. This trend was also observed at 800 °C, as can be seen in Figure 3c. It was sometimes observed that outer layers of carbon were incomplete, but a single layer still remained screening the Pt surface (yellow annotation).

Figure 4 shows representative AC-TEM images for different nitrogen precursor concentration from 0.5% to 4.0%. At 400 °C (Figure 4a,b), monolayer dominant coverage was observed regardless of nitrogen precursor concentration. By contrast, for the 4% nitrogen precursor sample (Figure 4b), thicker amorphous shells

are observed. This thicker amorphous shell was found to sometimes thin down to monolayer thicknesses (yellow arrow), although areas where the Pt surface was completely exposed (red arrows) were typically found in regions of regular crystalline monolayer encapsulation. At 800 °C (Figure 4c,d), it can be qualitatively seen that increasing the N precursor concentration results in the amorphous encapsulating layers seen for N 0.5% losing their crystallinity further, with the images shown in Figure 4c typically showing a greater degree of regularity to those in Figure 4d. Some noncorrected, HR-TEM images of Pt−Gr sample treated with N 2.0% concentration are shown in Supporting Information Figure S4, demonstrating 1−2 layer graphene coverage.

The morphological evolution of Pt−Gr core−shells synthesized under different conditions is summarized in Figure 5. The shell layer number was quantified by comparing the relative coverage of Pt surfaces with graphitic and amorphous carbon (Figure 5a). A clear decrease in the crystallinity of the encapsulating layer is observed with synthesis temperature and nitrogen precursor concentration. Figure 5b,c contrast the variation in the shell thickness for nitrogen precursor concentrations of 0.5% and 4.0%. In contrast to the
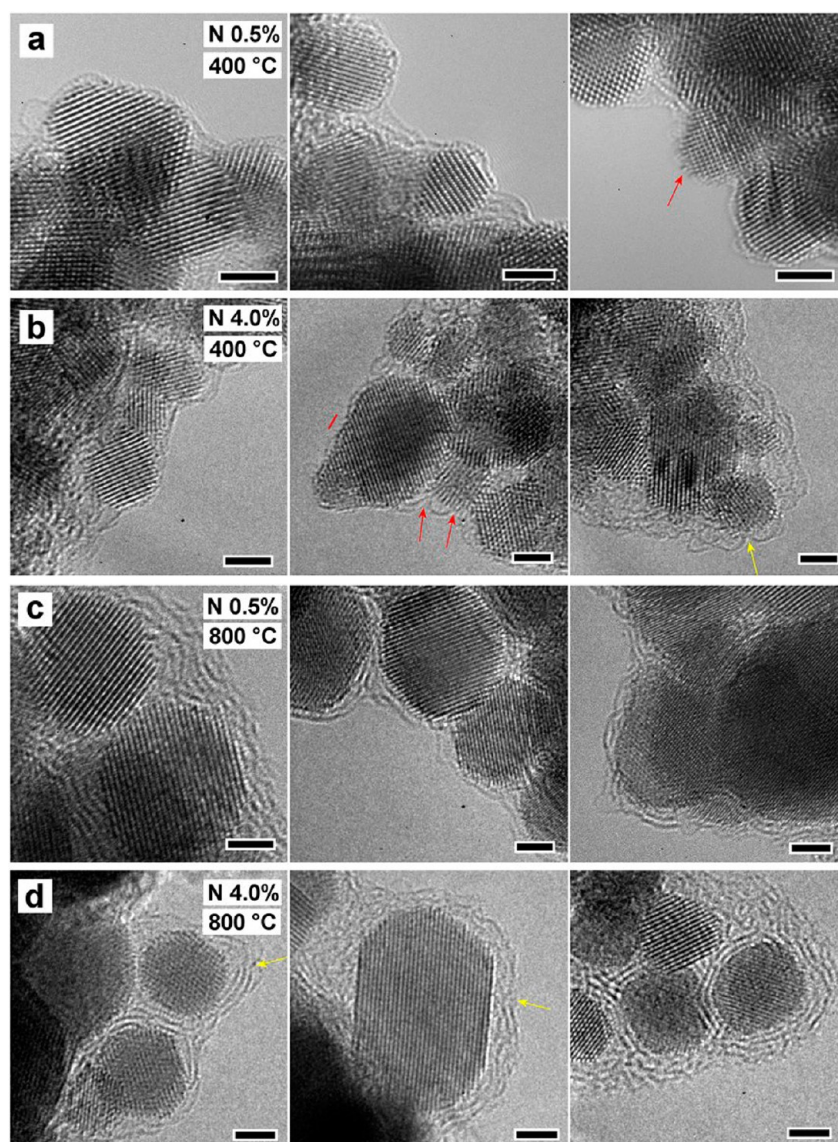
Figure 4. AC-TEM images showing the effect of nitrogen precursor concentration on Pt−Gr core−shells. Images are taken from samples synthesized at 400 °C (a and b) and 800 °C (c and d). Yellow annotations indicate the areas with incomplete shell growth. Red annotations indicate the exposure of bare Pt surface. Scale bars are 2 nm.

monolayer dominant coverage at 400 °C, multilayered amorphous carbon encapsulation predominates at higher temperatures. A similar shift toward amorphous encapsulation can be observed at high nitrogen precursor concentration. At 400 °C, monolayer graphene was almost exclusively observed for the 0.5% nitrogen precursor condition, but reduced to less than half for the N 4.0% condition, with greater portions of amorphous carbon encapsulation found. The size distribution of nanoparticles was also measured from the AC-TEM data (Figure 5d). Nanoparticle size was determined by fitting ellipses to individual particles to yield a characteristic diameter (the average of the semimajor and semiminor diameters), and the mean particle size determined by fitting a log-normal to the distribution (Supporting Information Figure S5). The plot shows an increase in particle size with synthesis temperature,

as expected, which can be attributed to the sintering of particles (see Supporting Information Figure S6).[29]

For more detailed characterization of defect structures in carbon shells, high magnification AC-TEM imaging was performed. Figure 6a shows smoothed AC-TEM image of a pair Pt−Gr nanocrystals. A magnified false color view of the boxed area is shown in Figure 6b. The false color shows the graphene layers as a dark band. Label 1 shows the graphene film having detached from the Pt surface, forming a small fold. This could explain the adjacent gap in the graphene encapsulation (label 2). The region indicated with label 3 shows several angstrom scale gaps. This contrasts with the uniform dark band of pristine graphene, as seen on the neighboring Pt−Gr crystal (label 4). A small protrusion of the graphene encapsulation is observed at label 5. However, there is also a graphene
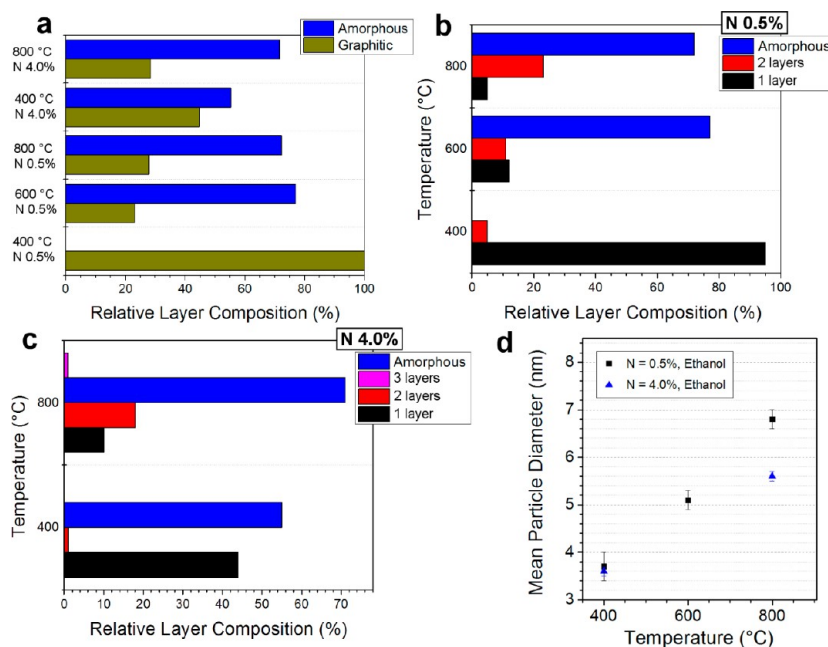
Figure 5. (a) Composition of encapsulating graphitic or amorphous layer for particular synthesis conditions. This is broken down into layer thickness in (b) and (c), for N precursor concentration by volume of 0.5% and 4.0%, respectively. (d) Mean nanoparticle diameter determined for various temperatures, solvent precursors and N %.
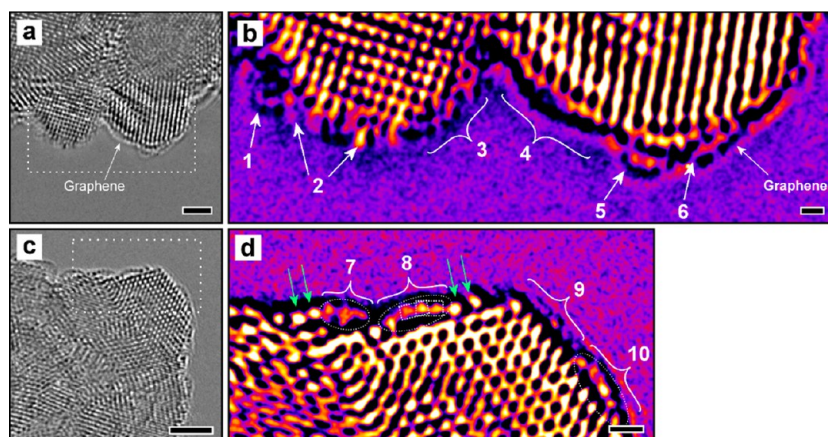

Figure 6. (a) Low magnification smoothed AC-TEM image of Pt–Gr (400 °C, N 0.5% with ethanol). Scale bar is 2 nm. (b) High magnification, false color view of the boxed region in (a). The outer black areas correspond to graphene (indicated), and the numbers refer to features of interest discussed in the main text. Scale bar is 0.5 nm. (c) Low magnification smoothed AC-TEM image of Pt–Gr (400 °C, N 0.5% with ethanol). Scale bar is 2 nm. (d) High magnification, false color view of the boxed region in (a). The circled areas indicate graphene coverage, green arrows denote isolated Pt atoms, and the numbers refer to features of interest discussed in the main text. Scale bar is 0.5 nm.

layer passing underneath. At label 6, the outer layer can be seen to apparently fold underneath another graphene layer. This is evidence for adjacent graphene grains interconnecting *via* overlap.[30] A further high magnification study is presented in Figure 6c,d. The boxed region in Figure 6c is magnified in Figure 6d, which shows a Pt crystal surface with some graphene coverage. The contrast for the graphene is different from Figure 6b, with the graphene appearing as a fainter orange than the Pt crystal. The regions of graphene coverage are circled and labeled 7, 8, and 10. Green arrows indicate single Pt atoms on the crystal surface, which reside at the termination of graphene layers labeled 7 and 8. The region labeled 9 shows no graphene coverage, with the Pt surface exposed to the environment.

Cyclic voltammetry of Pt–Gr core–shells of 0, 0.5, 2, and 4% nitrogen precursor concentration was performed in order to evaluate the effective electrochemical active surface (EAS) of Pt–Gr core–shell structures. Representative cyclic voltammograms are presented in Figure 7b–e for Pt–Gr core–shells synthesized from ethanol (carbon precursor) and pyridine (nitrogen precursor) at 400 °C. A commercially
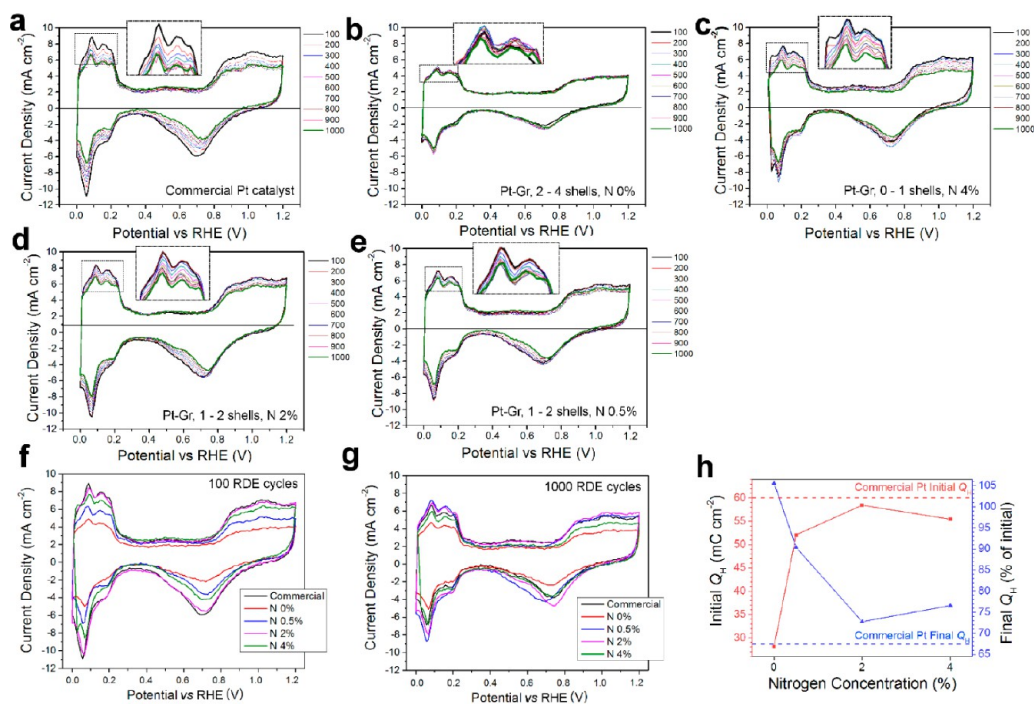
Figure 7. Cyclic voltammograms of various catalysts after undergoing increasing levels of RDE cycling (100−1000 cycles). (a) Commercially available Pt nanocrystal catalyst. (b) Pt−Gr core−shell catalyst with approximately 2−4 graphene shells (No N-addition). (c) Pt−Gr core−shell with 0−1 graphene shells (N 4% with ethanol), and Pt−Gr core−shell with 1−2 graphene shells with (d) N 2% and (e) N 0.5% with ethanol. The CV data for each sample after (f) 100 and (g) 1000 RDE cycles. (h) Initial Q_H, taken after the first 100 RDE cycles, and final Q_H, after 1000 RDE cycles, for samples with varying nitrogen precursor concentration. The corresponding commercial Pt values are marked with dotted lines.

available Pt catalyst (HiSPEC 4000, Johnson-Matthey, 40 wt % Pt on carbon black) was also analyzed as a reference (Figure 7a). The rate of catalyst degradation is given with cycle number, 100−1000 cycles, in the magnified views of Figure 7a−e. The 0% nitrogen, nondoped graphene encapsulated sample without pyridine precursor (Figure 7b) clearly shows little change with cycle number in comparison to the other samples. To compare the catalytic performance and degradation behavior across the samples, we collected voltammograms of all samples after 100 and 1000 RDE cycles in Figure 7, panels f and g, respectively. The performance of the commercial platinum sample is higher than that of graphene encapsulated samples after just 100 cycles; however, its performance relative to the others decays by 1000 cycles due to the various degradation mechanisms that act upon it. The graphene encapsulated samples show better performance after 1000 cycles with the best performance from the 0.5% nitrogen precursor sample.

A more rigorous and quantitative comparison of catalytic behavior was obtained by the comparison of their EAS, which is directly proportional to the Coulombic charge for hydrogen desorption, Q_H, directly extracted from the measured voltammograms.[31] The mean Q_H values from multiple repeat CV experiments performed on the Pt−Gr samples of interest were used to plot Figure 7h, which illustrate the effect of the graphene shell structure and thickness,

as influenced by nitrogen addition, on both catalyst efficiency and lifespan. The peak catalyst efficiency can be considered to be the EAS available after only a brief period of catalyst use, which was taken to be after 100 RDE cycles. To measure the rate of catalyst degradation, we considered the percentage EAS left after 1000 RDE cycles also.

The graphene shells can be seen to play two significant roles; first they severely limit overall catalyst efficiency unless nitrogen precursor is supplied during synthesis. The least efficient sample, where no nitrogen was supplied (N = 0%), demonstrated an average Q_H of just 28 ± 1 mC cm^{-2} at 100 RDE cycles. The inclusion of nitrogen precursor resulted in a noticeable rise in Pt−Gr hydrogen desorption, effectively matching the commercial grade Pt at N precursor volume percentages of 2%. Second, the growth of graphene shells on the Pt significantly increases the effective lifetime of the catalyst. In the pristine graphene encapsulated catalyst, the catalytic performance does not degrade until 1000 RDE cycles. This robust stabilization effect becomes steadily weaker with increasing nitrogen precursor concentration. An approximate compromise between performance and durability can be taken at the crossover of the two plots in Figure 7h, *i.e.*, N precursor concentration of ∼0.5% by volume.

Considering the previously presented AC-TEM data, it is evident that addition of nitrogen containing precursor results in imperfect and porous graphene
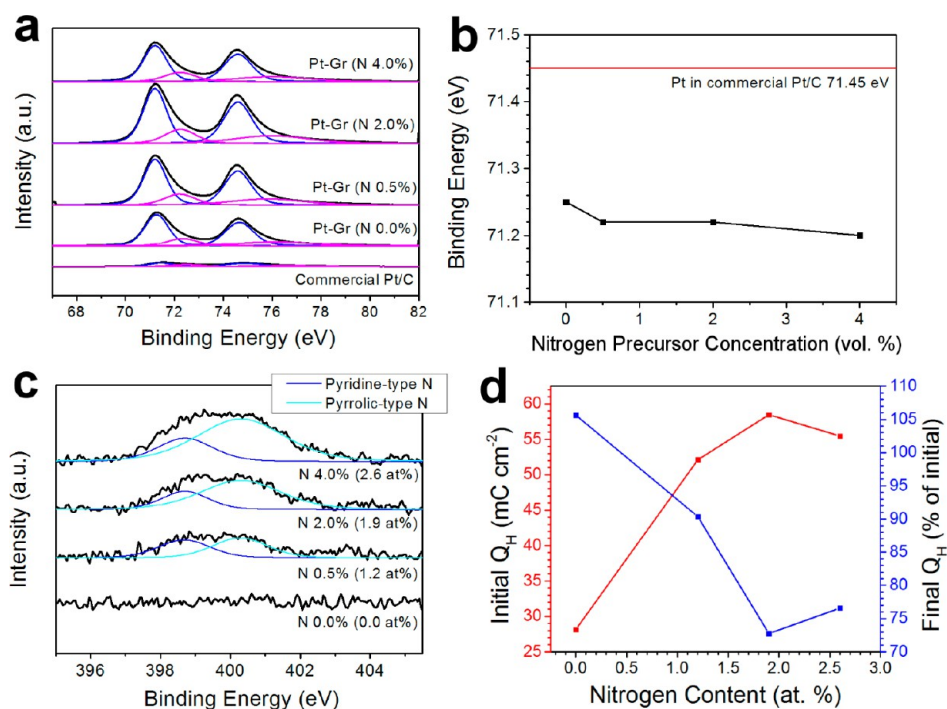
Figure 8. XPS spectra of Pt–Gr and commercial Pt/carbon black. (a) Binding energy of Pt 4f and (b) binding energy variation of Pt 4f$^{7/2}$ with nitrogen precursor concentration. (c) XPS spectra of nitrogen 1s and extracted nitrogen atomic %. (d) Relation of % atomic N content to Pt–Gr catalyst performance, both peak (initial) and degradation (final, % of initial).

encapsulation around Pt cores. The porous nature allows reactants to readily access the Pt catalyst surface. The AC-TEM images shown in Figure 4 demonstrate the porous nature of the graphene grown under the presence of nitrogen, with significant increases in the amorphous morphology and the numbers of gaps in the encapsulating layer. The reactants are thus able to access the Pt surface by permeating through the pores in the graphene shells, while the remaining shell still acts as an effective shield. As reported elsewhere,[19] encapsulation of Pt with graphitic outer shells acts to protect the Pt core from the various degradation mechanisms acting on the catalyst layer inside a fuel cell. Graphitic shells may directly shield the Pt from the hostile environment and prevent them from agglomerating *via* Ostwald ripening processes. However, adding defects to the graphene will allow the passage of atomic species, as has been previously shown for metallic atoms in graphene oxide.[32]

Of particular relevance for the cyclic voltammetry experiments performed here is the well documented problem of Pt dissolving in sulfuric acid environments; subjecting the Pt to the oscillating potentials found in electrochemical systems leads to the formation of an oxide layer, which is likely dependent on the oxidation and subsequent reduction of the Pt surface through the potential sweeps.[33,34] The graphene envelope we employ assists in protecting the Pt core from these negative effects. However, encapsulation also leads to the problem of the catalyst active sites being screened, effectively limiting the Pt EAS. This can be seen in the

cyclic voltammetry data, with the sample not subjected to a nitrogen containing precursor during growth having the worst catalytic performance, as characterized by Q_H. Adding a low concentration of nitrogen precursor during synthesis was found to improve Q_H significantly, due to the resulting defects in the graphene shell, although at the cost of reducing the efficacy of the shielding effect of the graphene. From the AC-TEM data presented in Figure 4 it can be seen that at 0.5% pyridine concentration the graphene shell is observed to only partially cover the Pt surface, leaving enough Pt exposed to act effectively as a catalyst but still leaving majority graphene coverage to protect the nanoparticle. Increasing the N precursor concentration further leads to the decrease in the protection effect of the graphene envelope, as expected, however does not improve the overall catalyst performance even after only a brief set of 100 RDE cycles. We suggest that this is due to the conversion of graphene to amorphous carbon at higher N concentrations that is observed in our AC-TEM data in Figure 4, which is distinct from the porous graphene encapsulation found at lower N concentrations. Thus, rather than improving the porosity of the graphene, increasing N merely leads to a consistently amorphous coating.

To confirm our proposed porous shell mechanism, X-ray photoelectron spectroscopy (XPS) was performed on the Pt–Gr core–shells, and also on a commercial Pt catalyst for reference. To eliminate any influence graphene may have in tuning Pt electronic properties, we can use the XPS spectra (Figure 8a) to determine the

binding energy of the Pt to the graphene shell (Pt—Gr core—shell samples) or the supporting carbon black (commercial Pt/C) (Figure 8b). These show that there is only a small 0.2 eV shift in the Pt peaks, suggesting Pt interacting with graphitic as opposed to amorphous carbon has at most only a slight impact on catalytic activity.

An important consideration is that nitrogen doped graphene is itself an effective catalyst.[35] The one-step nature of N-doped Pt—Gr core—shells does not lend itself to the synthesis of an equivalent N-doped graphene sample without any Pt content that might act as a suitable control sample to account for this. Instead, we analyzed the atomic % nitrogen content of the various Pt—Gr core—shells synthesized, and compared this to the measured catalytic performance. If the N-doped graphene itself was having a significant catalytic effect, we would expect two results: (i) that peak (initial) catalytic activity would correlate with nitrogen content, and (ii) that there would be less degradation in performance with higher nitrogen content. XPS spectra (Figure 8c) were taken to obtain the N atomic %, which is plotted *versus* initial and final Q_H in Figure 8d, as obtained from the CV data in Figure 7. The peak catalytic activity, as characterized by initial Q_H, does not strongly correlate with N atom % at higher percentages, suggesting that nitrogen doped graphene itself is not the dominant catalytic effect. However, the literature is somewhat unclear on the importance of overall nitrogen atom %, due to the various types of nitrogen bonding (pyridinic, pyrrolic, quarternary) and the complex, multipath electrochemistry for catalysis.[35,36] A more definitive finding in the literature has been that nitrogen doped graphene is an exceptionally resilient catalyst, with a 1000 cycle accelerated stress test showing no degradation,[37] as with our nondoped Pt—Gr core—shell catalyst (Figure 7b). The level of degradation we see with our doped samples, while improved over bare Pt, is still significant, as shown by the final Q_H in Figure 8d, suggesting that the Pt has more significant role in catalysis than the N-doped graphene.

CONCLUSION

We have presented high durability Pt—Gr core—shell nanoparticles synthesized by single step thermal evaporation process for use in PEMFCs. The synthesis can be performed with a range of carbon precursors at different temperatures. Low temperatures of ~400 °C yield graphene shells 1—2 layers thick. The graphene shells greatly improve the lifetime of the catalyst, but at the cost of inhibited performance. Pyridine addition during synthesis, in the range of 0.5% to 4% by volume, was found to change the graphene shell morphology, preventing the full formation of graphene shells around the Pt core and introducing defects. We propose that this mechanism allows for the engineering of the protective graphene shell to include porous defects, thus permitting the ingress of reactants to the catalytic Pt surface. Thus, through nitrogen addition it is possible to maintain the benefits that the graphene shielding affords while significantly minimizing its negative effect on catalyst performance.

METHODS

Pt—Gr Core—Shell Synthesis. Pt precursor (2 g, MeCpPtMe₃; methyl trimethyl cyclopentadienyl Pt) is vaporized by heating up the chamber (pyrex, 100 mL) up to 60 °C. The Pt vapor was transferred to the quartz tube (2-in. diameter) for the core—shell synthesis by a nitrogen carrier gas (flow rate 20 sccm). Graphene shell growth was achieved using various carbon precursors, such as CH_4, C_2H_2, EtOH and CH_3COCH_3. Gaseous precursors were diluted with N_2 up to 5% by volume, then transferred to a quartz tube. Liquid precursors such as EtOH and CH_3COCH_3 were vaporized in another Pyrex chamber at 75 and 50 °C, respectively, then transferred by N_2 carrier gas (flow rate 60 sccm) to the quartz tube. Both the Pt and carbon precursors in their gas phases are simultaneously injected into a quartz tube with additional N_2 gas (70 sccm), which is heated to a temperature between 400 and 1100 °C for core—shell synthesis.

For the collection of Pt—Gr nano particles, carbon paper (Toray, TGP-H-060, 190 μm thickness) was set on the quartz filter. The SEM images in Supporting Information Figure S2 show Pt—Gr particles are deposited on carbon paper in a highly dispersed manner, which can be directly used as a fuel cell electrode without any treatment.

TEM Imaging. Pt—Gr particles were collected from the carbon paper, and aberration corrected microscopy was performed on Oxford's JEOL 2200MCO double imaging and probe corrected AC-TEM. An accelerating voltage of 80 kV was used to minimize electron beam induced damage to the graphene coating. Samples were prepared by brief sonication in ethanol, before drop-casting to a lacey carbon grid. ImageJ was used to generate false color images by using a "Fire" look-up table.

Noncorrected HR-TEM observation of Figure 2 and Supporting Information Figures S7 and S8 was performed on Tecnai F30 Super twin of FEI with the accelerating voltage of 200 kV.

Raman Spectroscopy Measurements. Raman spectra of each Pt—Gr samples were obtained at room temperature with a Jobin-Yvon HR800 Raman system with a laser of 514 nm.

XRD Measurements. XRD spectra indicated in Supporting Information Figure S3 were collected on Bruker D8 Advance System with Cu Kα radiation (wavelength λ = 0.15147 nm) at a scan rate of 10 s deg^{-1}.

Cyclic Voltammetry Measurements. The electrochemical activities of Pt—Gr catalysts were measured using a potentiostat (BioLogic, SP-50) equipped with rotating ring disk electrode (RRDE). A saturated Ag/AgCl was used as the reference electrode and was calibrated with respect to a reversible hydrogen electrode (RHE). A glassy carbon disk (3 mm in diameter) and Pt wire were used as the working electrode and counter electrodes, respectively. In the RRDE system, the working electrode was prepared by loading catalyst ink (0.2 mg Pt cm^{-2}; a mixture of 2 mg catalyst, 5 μL Nafion solution (5 wt %, DuPont) and 1 mL ethanol) on the glassy carbon electrode. RRDE measurements were conducted in an H_2SO_4 solution (0.5 M) at 25 °C using a scan rate of 5 mV s^{-1} and a rotation speed of 1500 rpm.

X-ray Photoelectron Spectroscopy Measurements. X-ray photoelectron spectroscopy (XPS) was carried out using K-Alpha X-ray photoelectron spectrometer system (Thermo Scientific).

Samples were irradiated by a monochromatic Al Kα X-ray source. Peak fittings were accomplished using Avantage. Charge referencing was done with the carbon (C 1s) peak position of 284.5 eV.

SEM Measurements. SEM images of Pt–Gr particles as deposited on carbon paper (Supporting Information Figure S1) were obtained on HITACHI S-4700 at an accelerating voltage of 20 kV.

Conflict of Interest: The authors declare no competing financial interest.

Supporting Information Available: Schematic of the experimental setup; photograph of the carbon paper substrate; SEM images demonstrating the dispersal of as-collected Pt nanoparticles on the carbon paper; X-ray diffraction spectrum of the Pt–Gr core–shells; Raman profiles for different temperatures, and peak position and intensity analysis, for different carbon precursors; TEM images of Pt–Gr (N 2%) synthesized at 400 °C using ethanol as C-precursor; histograms and log-normal fits to obtain the mean particle diameters; AC-TEM image of two Pt particles sintering together (400 °C, N 0.5%); TEM observation of used catalysts. The Supporting Information is available free of charge on the ACS Publications website at DOI: 10.1021/acsnano.5b00678.

REFERENCES AND NOTES

1. Li, Y.; Zhou, W.; Wang, H.; Xie, L.; Liang, Y.; Wei, F.; Idrobo, J.-C.; Pennycook, S. J.; Dai, H. An Oxygen Reduction Electrocatalyst Based on Carbon Nanotube-Graphene Complexes. *Nat. Nanotechnol.* **2012**, *7*, 394–400.

2. Jaramillo, T. F.; Jørgensen, K. P.; Bonde, J.; Nielsen, J. H.; Horch, S.; Chorkendorff, I. Identification of Active Edge Sites for Electrochemical H$_2$ Evolution from MoS$_2$ Nanocatalysts. *Science* **2007**, *317*, 100–102.

3. Chen, Z.; Higgins, D.; Yu, A.; Zhang, L.; Zhang, J. A Review on Non-Precious Metal Electrocatalysts for PEM Fuel Cells. *Energy Environ. Sci.* **2011**, *4*, 3167.

4. Winter, M.; Brodd, R. J. What Are Batteries, Fuel Cells, and Supercapacitors? *Chem. Rev.* **2004**, *104*, 4245–4270.

5. Zhang, S.; Yuan, X.-Z.; Hin, J. N. C.; Wang, H.; Friedrich, K. A.; Schulze, M. A Review of Platinum-Based Catalyst Layer Degradation in Proton Exchange Membrane Fuel Cells. *J. Power Sources* **2009**, *194*, 588–600.

6. Darling, R. M.; Meyers, J. P. Kinetic Model of Platinum Dissolution in PEMFCs. *J. Electrochem. Soc.* **2003**, *150*, A1523.

7. Wu, J.; Yuan, X. Z.; Martin, J. J.; Wang, H.; Zhang, J.; Shen, J.; Wu, S.; Merida, W. A Review of PEM Fuel Cell Durability: Degradation Mechanisms and Mitigation Strategies. *J. Power Sources* **2008**, *184*, 104–119.

8. Wang, D.; Xin, H. L.; Hovden, R.; Wang, H.; Yu, Y.; Muller, D. A.; DiSalvo, F. J.; Abruña, H. D. Structurally Ordered Intermetallic Platinum-Cobalt Core-Shell Nanoparticles with Enhanced Activity and Stability as Oxygen Reduction Electrocatalysts. *Nat. Mater.* **2013**, *12*, 81–87.

9. Antolini, E.; Salgado, J. R. C.; Gonzalez, E. R. The Stability of Pt–M (M=first Row Transition Metal) Alloy Catalysts and Its Effect on the Activity in Low Temperature Fuel Cells. *J. Power Sources* **2006**, *160*, 957–968.

10. Strasser, P.; Koh, S.; Anniyev, T.; Greeley, J.; More, K.; Yu, C.; Liu, Z.; Kaya, S.; Nordlund, D.; Ogasawara, H.; et al. Lattice-Strain Control of the Activity in Dealloyed Core-Shell Fuel Cell Catalysts. *Nat. Chem.* **2010**, *2*, 454–460.

11. Stamenkovic, V. R.; Mun, B. S.; Arenz, M.; Mayrhofer, K. J. J.; Lucas, C. A.; Wang, G.; Ross, P. N.; Markovic, N. M. Trends in Electrocatalysis on Extended and Nanoscale Pt-Bimetallic Alloy Surfaces. *Nat. Mater.* **2007**, *6*, 241–247.

12. Kim, J.; Lee, Y.; Sun, S. Structurally Ordered FePt Nanoparticles and Their Enhanced Catalysis for Oxygen Reduction Reaction. *J. Am. Chem. Soc.* **2010**, *132*, 4996–4997.

13. Stamenkovic, V. R.; Mun, B. S.; Mayrhofer, K. J. J.; Ross, P. N.; Markovic, N. M. Effect of Surface Composition on Electronic Structure, Stability, and Electrocatalytic Properties of Pt-Transition Metal Alloys: Pt-Skin *versus* Pt-Skeleton Surfaces. *J. Am. Chem. Soc.* **2006**, *128*, 8813–8819.

14. Hwang, S. J.; Yoo, S. J.; Jang, S.; Lim, T.; Hong, S. A.; Kim, S. Ternary Pt–Fe–Co Alloy Electrocatalysts Prepared by Electrodeposition: Elucidating the Roles of Fe and Co in the Oxygen Reduction Reaction. *J. Phys. Chem. C* **2011**, *115*, 2483–2488.

15. Xin, H. L.; Mundy, J. A.; Liu, Z.; Cabezas, R.; Hovden, R.; Kourkoutis, L. F.; Zhang, J.; Subramanian, N. P.; Makharia, R.; Wagner, F. T.; et al. Atomic-Resolution Spectroscopic Imaging of Ensembles of Nanocatalyst Particles across the Life of a Fuel Cell. *Nano Lett.* **2012**, *12*, 490–497.

16. Wang, J. X.; Inada, H.; Wu, L.; Zhu, Y.; Choi, Y.; Liu, P.; Zhou, W.-P.; Adzic, R. R. Oxygen Reduction on Well-Defined Core-Shell Nanocatalysts: Particle Size, Facet, and Pt Shell Thickness Effects. *J. Am. Chem. Soc.* **2009**, *131*, 17298–17302.

17. Sasaki, K.; Naohara, H.; Cai, Y.; Choi, Y. M.; Liu, P.; Vukmirovic, M. B.; Wang, J. X.; Adzic, R. R. Core-Protected Platinum Monolayer Shell High-Stability Electrocatalysts for Fuel-Cell Cathodes. *Angew. Chem.* **2010**, *49*, 8602–8607.

18. Gong, K.; Su, D.; Adzic, R. R. Platinum-Monolayer Shell on AuNi(0.5)Fe Nanoparticle Core Electrocatalyst with High Activity and Stability for the Oxygen Reduction Reaction. *J. Am. Chem. Soc.* **2010**, *132*, 14364–14366.

19. Wen, Z.; Liu, J.; Li, J. Core/Shell Pt/C Nanoparticles Embedded in Mesoporous Carbon as a Methanol-Tolerant Cathode Catalyst in Direct Methanol Fuel Cells. *Adv. Mater.* **2008**, *20*, 743–747.

20. Gao, L.; Ren, W.; Xu, H.; Jin, L.; Wang, Z.; Ma, T.; Ma, L.-P.; Zhang, Z.; Fu, Q.; Peng, L.-M.; et al. Repeated Growth and Bubbling Transfer of Graphene with Millimetre-Size Single-Crystal Grains Using Platinum. *Nat. Commun.* **2012**, *3*, 699.

21. Sutter, P.; Sadowski, J. T.; Sutter, E. Graphene on Pt(111): Growth and Substrate Interaction. *Phys. Rev. B* **2009**, *80*, 245411.

22. Lang, B. A LEED Study of the Deposition of Carbon on Platinum Crystal Surfaces. *Surf. Sci.* **1975**, *53*, 317–329.

23. Robertson, J. Heterogeneous Catalysis Model of Growth Mechanisms of Carbon Nanotubes, Graphene and Silicon Nanowires. *J. Mater. Chem.* **2012**, *22*, 19858.

24. Meyer, J. C.; Geim, A. K.; Katsnelson, M. I.; Novoselov, K. S.; Booth, T. J.; Roth, S. The Structure of Suspended Graphene Sheets. *Nature* **2007**, *446*, 60–63.

25. Robertson, A. W.; Warner, J. H. Hexagonal Single Crystal Domains of Few-Layer Graphene on Copper Foils. *Nano Lett.* **2011**, *11*, 1182–1189.

26. Ferrari, A. C.; Robertson, J. Raman Spectroscopy of Amorphous, Nanostructured, Diamond-like Carbon, and Nanodiamond. *Philos. Trans. R. Soc., A* **2004**, *362*, 2477–2512.

27. Ferrari, A. C.; Meyer, J. C.; Scardaci, V.; Casiraghi, C.; Lazzeri, M.; Mauri, F.; Piscanec, S.; Jiang, D.; Novoselov, K. S.; Roth, S.; et al. Raman Spectrum of Graphene and Graphene Layers. *Phys. Rev. Lett.* **2006**, *97*, 187401.

28. Ferrari, A.; Robertson, J. Interpretation of Raman Spectra of Disordered and Amorphous Carbon. *Phys. Rev. B* **2000**, *61*, 14095–14107.

29. Cichocka, M. O.; Zhao, J.; Bachmatiuk, A.; Quang, H. T.; Gorantla, S. M.; Gonzalez-Martinez, I. G.; Fu, L.; Eckert, J.; Warner, J. H.; Rümmeli, M. H. *In Situ* Observations of Pt Nanoparticles Coalescing inside Carbon Nanotubes. *RSC Adv.* **2014**, *4*, 49442–49445.

30. Robertson, A. W.; Bachmatiuk, A.; Wu, Y. A.; Schäffel, F.; Rellinghaus, B.; Büchner, B.; Rümmeli, M. H.; Warner, J. H. Atomic Structure of Interconnected Few-Layer Graphene Domains. *ACS Nano* **2011**, *5*, 6610–6618.

31. Pozio, A.; De Francesco, M.; Cemmi, A. Comparison of High Surface Pt/C Catalysts by Cyclic Voltammetry. *J. Power Sources* **2002**, *105*, 13–19.

32. Ogata, C.; Koinuma, M.; Hatakeyama, K.; Tateishi, H.; Asrori, M. Z.; Taniguchi, T.; Funatsu, A.; Matsumoto, Y. Metal Permeation into Multi-Layered Graphene Oxide. *Sci. Rep.* **2014**, *4*, 3647.

33. Topalov, A. A.; Cherevko, S.; Zeradjanin, A. R.; Meier, J. C.; Katsounaros, I.; Mayrhofer, K. J. J. Towards a Comprehensive Understanding of Platinum Dissolution in Acidic Media. *Chem. Sci.* **2014**, *5*, 631.

34. Sugawara, Y.; Okayasu, T.; Yadav, A. P.; Nishikata, A.; Tsuru, T. Dissolution Mechanism of Platinum in Sulfuric Acid Solution. *J. Electrochem. Soc.* **2012**, *159*, F779–F786.

35. Wang, H.; Maiyalagan, T.; Wang, X. Review on Recent Progress in Nitrogen-Doped Graphene: Synthesis, Characterization, and Its Potential Applications. *ACS Catal.* **2012**, *2*, 781–794.

36. Luo, Z.; Lim, S.; Tian, Z.; Shang, J.; Lai, L.; MacDonald, B.; Fu, C.; Shen, Z.; Yu, T.; Lin, J. Pyridinic N Doped Graphene: Synthesis, Electronic Structure, and Electrocatalytic Property. *J. Mater. Chem.* **2011**, *21*, 8038.

37. Shao, Y.; Zhang, S.; Engelhard, M. H.; Li, G.; Shao, G.; Wang, Y.; Liu, J.; Aksay, I. a.; Lin, Y. Nitrogen-Doped Graphene and Its Electrochemical Applications. *J. Mater. Chem.* **2010**, *20*, 7491.